

Transient behavior of the thermocapillary migration of drops under the influence of deformation

L. Chang, Z. Yin,* and W. Hu

*National Microgravity Laboratory, Institute of Mechanics,
Chinese Academy of Sciences, Beijing 100190, P.R.China*

(Dated: December 8, 2011)

Abstract

The transient thermocapillary migration of drops with nontrivial deformation is studied. The finite difference method is employed to solve the incompressible Navier-Stokes equations coupled with the energy equation; the front-tracking method is adopted to track the moving deformable drop interface. In the hot region, deformations of drops increase with the decrease of interfacial tensions. In order to indicate the temperature impact on the interfacial tension, a local capillary number (Ca_l) is introduced. It is found that, when the drop density is smaller/larger than that of the bulk fluid, the drop velocity decreases/increases with the increase of the drop deformation.

*Electronic address: zhaohua.yin@imech.ac.cn

I. INTRODUCTION

Thermocapillary migration, which is induced by the variance of the interfacial tension when a temperature gradient is imposed on the bulk fluid, is an important phenomenon in drop/bubble transportation. With the development of aeronautics and astronautics, it is necessary to study the thermocapillary motion because of its practical roles in the material processing, and the management of heat and fluids in space [1, 2]. In most studies on the thermocapillary motion, it is assumed that the interfacial tension linearly depends on the temperature:

$$\sigma(T) = \sigma_0 + \sigma_T(T - T_0), \quad (1)$$

where the constant σ_T is the interfacial tension coefficient of temperature, and σ_0 the interfacial tension at the reference temperature T_0 .

Considering the balance between the capillary force and viscosity on the bubble or drop, the reference velocity can be defined as

$$U = |\sigma_T| |\nabla T_\infty| R_0 / \mu_1,$$

in which $|\nabla T_\infty|$ is the temperature gradient imposed on bulk fluid (the subscript 1 represented), μ the viscosity, and R_0 the radius of the spherical drop/bubble.

	$\sigma_0(10^{-3}N/m)$	$\sigma_T(10^{-3}N/(m \cdot K))$
Gas bubble/Silicone oil[3]	17.3	-0.061
Fc-75 drop/Silicone oil[3]	3.47	-0.036
Monotectic alloy[4]	5.7	-0.23

TABLE I: Typical interfacial tensions and their temperature coefficients.

The capillary number is defined as

$$Ca = \mu_1 U / \sigma_0 = |\sigma_T| |\nabla T_\infty| R_0 / \sigma_0.$$

In most cases, the Ca numbers in thermocapillary migration are small (0.01 or less, e.g., the materials in the first two lines of Table 1), and the deformations of drops are also very small. Therefore, previous studies usually assumed drops to be nondeformable [5]. However, in practice, there are many situations where the interface tension is very small,

or where the deformation introduced by capillary effect is very large. For the case of the preparation of monotectic alloys in micro-gravity conditions [6], the Ca number of the Al-based alloy $(Al_{34.5}Bi_{65.5})_{95}Sn_5$ is 0.12 at the temperature of 1200K if $R_0 = 300\mu m$ and $|\nabla T_\infty| = 100K/cm$ [7] (see the third line in Table 1). Such a big Ca number can cause obvious deformation on the drop. Similar situations happen in the chemical flooding methods applied in enhanced oil recovery [8–12]. Finally, experiments in space also observed some slight deformation of fairly large bubbles [3]. Therefore, it is necessary to investigate the deformed drops with relatively large Ca 's or small interfacial tensions in the thermocapillary studies.

When inertia and thermal convections are neglected, the velocity of the spherical drop in thermocapillary motion is presented in the pioneering work of Young *et al.* [13]:

$$V_{YGB} = 2AU,$$

where

$$A = \frac{1}{(2 + 3\alpha)(2 + \lambda)}, \quad (2)$$

and $\alpha = \mu_2/\mu_1$ and $\lambda = k_2/k_1$ are the ratios of the kinematic viscosity and thermal conductivity between droplet (the subscript 2 represented) and background liquid, respectively.

There are a lot of investigations studying the thermocapillary motion, which are reviewed in [14, 15]. Most of the researches so far focus on the convection effects of inertia and energy, and only a few of them are about the drop/bubble deformation. When the thermal convection is very small, the exact solution of the momentum equation was provided in [16], where small inertial deformations of drops were also calculated. Under the same assumption, using the Lorentz reciprocal theorem, Haj-Hariri *et al.* calculated the small inertial deformations as well as the consequent correction on the temperature field and the migration velocity [17]. Later, the work is extended to moderate parameters in a steady-state numerical investigation [18]. It is concluded that even a small deformation will retard the motion of the drop, and the steady-state migration can still be reached even for large capillary numbers up to 0.5. However, the actual continuous decrease of the interfacial tension when the drop migrates to the hot region was not considered in their study. While taking this decrease into consideration, bubbles with large capillary numbers can not reach steady migrating states [19].

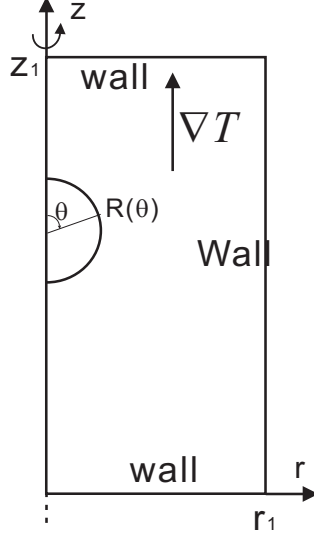


FIG. 1: The sketch of thermocapillary motion in the axisymmetric model.

According to our knowledge, transient migration behaviors due to drop deformation have never been reported before, which is the main topic in this work. This paper is arranged as follows: the governing equations and numerical methods are introduced in Section 2, the validation tests are presented in Section 3, and the results and discussions are in Section 4.

II. GOVERNING EQUATIONS AND NUMERICAL METHODS

In our axisymmetric simulation, the initially-spherical droplet with a radius of R_0 is surrounded by the bulk liquid, which is imposed on a constant temperature gradient along the z axis (Fig. 1). The calculated domain is $\Omega((r, z))$ ($r \in [0, r_1]$, $z \in [0, z_1]$), and the center of the droplet is at $r = 0$. The governing equations for the thermocapillary migration of droplets are:

$$\nabla \cdot \mathbf{u} = 0, \quad (3)$$

$$\frac{\partial(\rho \mathbf{u})}{\partial t} + \nabla \cdot (\rho \mathbf{u} \mathbf{u}) = -\nabla p + \nabla \cdot (\mu(\nabla \mathbf{u} + \nabla^T \mathbf{u})) + \mathbf{F}_\sigma, \quad (4)$$

$$\rho C_p \left(\frac{\partial T}{\partial t} + \mathbf{u} \cdot \nabla T \right) = \nabla \cdot (k \nabla T), \quad (5)$$

in which $\mathbf{u} = (v_r, v_z)$ is the velocity, ρ the density, p the pressure, and C_p the specific heat. \mathbf{F}_σ is the body force term due to the interfacial tension, and its axisymmetrical formula is presented in [20, 21]:

$$\mathbf{F}_\sigma = \int_B \delta(\mathbf{x} - \mathbf{x}_f) \left(\sigma \kappa \mathbf{n} + \frac{\partial \sigma}{\partial s} \boldsymbol{\tau} \right) ds. \quad (6)$$

Here, $\mathbf{x} = (r, z)$ is the space vector, $\mathbf{x}_f = (r_f, z_f)$ the position of the cell f on the interface B , and s the natural coordinate along the interface. $\mathbf{n} = (n_r, n_z)$ and $\boldsymbol{\tau}$ denote the normal and tangential unit vectors of the interface, respectively. $\kappa = \kappa_1 + \kappa_2$ is the sum of two principal curvatures of the interface, κ_1 is the in-plane curvature and κ_2 is given as [22]:

$$\kappa_2 = -\frac{n_r}{r_f}. \quad (7)$$

We defined nondimensional variables as follows:

$$\begin{aligned} \bar{\mathbf{u}} &= \mathbf{u}/U, \quad \bar{\mathbf{x}} = \mathbf{x}/R_0, \quad \bar{t} = t/(\frac{R_0}{U}), \quad \bar{p} = p/(\rho_1 U^2), \\ \bar{T} &= T/(|\nabla T_\infty| R_0), \quad \bar{\rho} = \rho/\rho_1, \quad \bar{\xi} = \rho_2/\rho_1, \quad \bar{\mu} = \mu/\mu_1, \\ \bar{k} &= k/k_1, \quad \bar{C}_p = C_p/C_{p1}, \quad \bar{\gamma} = C_{p2}/C_{p1}, \\ \bar{\mathbf{F}}_\sigma &= \mathbf{F}_\sigma R_0/(\rho_1 U^2), \quad Ma = \rho_1 C_{p1} U R_0/k_1. \end{aligned} \quad (8)$$

In total, the problem is governed by seven nondimensional parameters: $Re, Ma, Ca, \alpha, \lambda, \gamma$ and ξ . The nondimensional equations in the axisymmetrical model are:

$$\frac{\partial \bar{v}_r}{\partial \bar{r}} + \frac{\bar{v}_r}{\bar{r}} + \frac{\partial \bar{v}_z}{\partial \bar{z}} = 0, \quad (9)$$

$$\begin{aligned} \frac{\partial(\bar{\rho}\bar{v}_r)}{\partial \bar{t}} + \frac{1}{\bar{r}} \frac{\partial(\bar{r}\bar{\rho}\bar{v}_r\bar{v}_r)}{\partial \bar{r}} + \frac{\partial(\bar{\rho}\bar{v}_z\bar{v}_r)}{\partial \bar{z}} &= -\frac{\partial \bar{p}}{\partial \bar{r}} + \frac{1}{Re} \left[\frac{2}{\bar{r}} \frac{\partial}{\partial \bar{r}} (\bar{r}\bar{\mu}(\frac{\partial \bar{v}_r}{\partial \bar{r}})) + \frac{\partial}{\partial \bar{z}} (\bar{\mu}(\frac{\partial \bar{v}_r}{\partial \bar{z}} + \frac{\partial \bar{v}_z}{\partial \bar{r}})) - \frac{2\bar{\mu}\bar{v}_r}{\bar{r}^2} \right] \\ &\quad + \bar{F}_{\sigma r} \end{aligned} \quad (10)$$

$$\begin{aligned} \frac{\partial(\bar{\rho}\bar{v}_z)}{\partial \bar{t}} + \frac{1}{\bar{r}} \frac{\partial(\bar{r}\bar{\rho}\bar{v}_r\bar{v}_z)}{\partial \bar{r}} + \frac{\partial(\bar{\rho}\bar{v}_z\bar{v}_z)}{\partial \bar{z}} &= -\frac{\partial \bar{p}}{\partial \bar{z}} + \frac{1}{Re} \left[\frac{1}{\bar{r}} \frac{\partial}{\partial \bar{r}} (\bar{r}\bar{\mu}(\frac{\partial \bar{v}_z}{\partial \bar{r}} + \frac{\partial \bar{v}_r}{\partial \bar{z}})) + 2\frac{\partial}{\partial \bar{z}} (\bar{\mu}(\frac{\partial \bar{v}_z}{\partial \bar{z}})) \right] \\ &\quad + \bar{F}_{\sigma z} \end{aligned} \quad (11)$$

$$\bar{\rho}\bar{C}_p \left(\frac{\partial \bar{T}}{\partial \bar{t}} + \bar{v}_r \frac{\partial \bar{T}}{\partial \bar{r}} + \bar{v}_z \frac{\partial \bar{T}}{\partial \bar{z}} \right) = \frac{1}{Ma} \left[\frac{1}{\bar{r}} \frac{\partial}{\partial \bar{r}} (\bar{r}\bar{k} \frac{\partial \bar{T}}{\partial \bar{r}}) + \frac{\partial}{\partial \bar{z}} (\bar{k} \frac{\partial \bar{T}}{\partial \bar{z}}) \right]. \quad (12)$$

Using Eq. 1, the nondimensional interfacial tension term $\bar{\mathbf{F}}_\sigma$ can be written as:

$$\bar{\mathbf{F}}_\sigma = \int_B \delta(\bar{\mathbf{x}} - \bar{\mathbf{x}}_f) \left(\left(\frac{1}{ReCa} - \frac{1}{Re} (\bar{T} - \bar{T}_0) \right) \kappa \mathbf{n} - \frac{1}{Re} \frac{\partial \bar{T}}{\partial \bar{s}} \boldsymbol{\tau} \right) d\bar{s}. \quad (13)$$

Eqs. 9-12 are valid for both phases of the drop and the bulk fluid. The discontinuities of the physical parameters across the interface are handled with an indicator function (see [23] for more details). The governing equations are discretized by the second-order

center-difference method on fixed, staggered, Cartesian grids. The projection method [24] is adopted to solve the Navier-Stokes equations.

On the symmetric axis, the symmetrical condition is employed:

$$\bar{v}_r|_{\bar{r}=0} = 0, \quad \frac{\partial \bar{v}_z}{\partial \bar{r}}|_{\bar{r}=0} = 0, \quad \frac{\partial \bar{T}}{\partial \bar{r}}|_{\bar{r}=0} = 0, \quad (14)$$

and all other boundaries for velocities adopt rigid boundary conditions, and those for temperature use constant temperature boundary conditions. Following the tradition in this field, the initial conditions are:

$$\bar{v}_r|_{\bar{t}=0} = \bar{v}_z|_{\bar{t}=0} = 0, \quad \bar{T}|_{\bar{t}=0} = \bar{z}. \quad (15)$$

In the following, symbols without bars will be used to denote nondimensional values.

In addition, when the momentum equation is solved at each new time step, the front element f is supposed to have the same velocity (\mathbf{u}_f) as that of the surrounding fluid. In order to update the front with a conserved drop volume, a velocity correction Δu_n is imposed on \mathbf{u}_f in the normal direction (\mathbf{n}_f) of the element:

$$\Delta u_n = -\frac{\sum_f \Delta s_f \mathbf{u}_f \cdot \mathbf{n}_f}{\sum_f \Delta s_f}. \quad (16)$$

With this correction, the drop volume is almost conserved throughout our simulations with a maximum volume loss of less than 0.1% of the initial volume. By comparison, without the velocity correction, there will be about 2% loss at the simulating time $t = 20$.

The computing domain in this paper is $(r, z) \in [0, 6] \times [0, 24]$, and the resolution is 128×512 . The time step is 2×10^{-4} for most cases, and 1×10^{-4} for the $\xi = 0.01$ case in subsection 4.2.

III. THE VALIDATION OF THE COMPUTING PROGRAM

In tradition, the scaled deviation of the drop profile from the sphere is defined as

$$f(\theta) = R(\theta)/R_0 - 1,$$

where, the polar angle θ is measured from the front stagnation point and $R(\theta)$ denotes the distance between the interface and the mass center of the drop (Fig. 1).

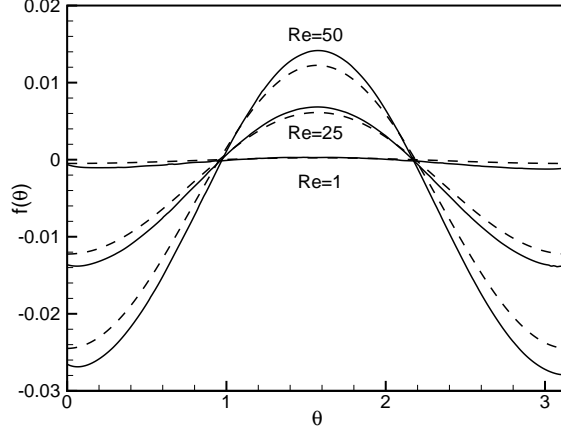


FIG. 2: Deviation of the drop profile from the sphere for $Ma = 1$, $Ca = 0.1$, $\alpha = \lambda = \xi = 0.5$, $\gamma = 0.25$, and Re as indicated. Dash line: the theoretical prediction in [17]; solid line: the present work.

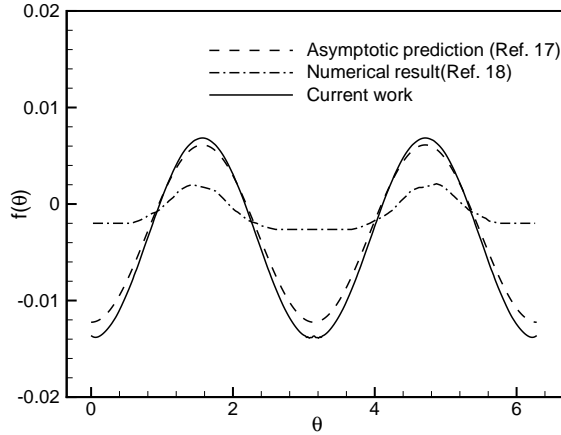


FIG. 3: Deviations of drop profiles from spheres in [17], [18], and this work, where $Re = 25$, $Ma = 1$, $Ca = 0.1$, $\alpha = \lambda = \xi = 0.5$, and $\gamma = 0.25$.

Before this work, there was a theoretical result of small inertial deformations of drops with small Ca and Re numbers [17]:

$$f(\theta) = \frac{3}{8}A^2ReCa(\xi - 1)(3\cos^2\theta - 1). \quad (17)$$

The earlier numerical simulation [18], however, used a different formula for the interfacial tension:

$$\mathbf{F}_\sigma = \int_B \delta(\mathbf{x} - \mathbf{x}_f) \left(\frac{1}{ReCa} \kappa \mathbf{n} - \frac{1}{Re} \frac{\partial T}{\partial s} \boldsymbol{\tau} \right) ds. \quad (18)$$

Compared with Eq. 13, the effect of capillary force in Eq. 18 was assumed constant on the normal direction of the interface, or, there is no decrease in the interfacial tension when the

droplet moves to the hotter region [18]. There are two distinguished differences between these two assumptions:

1. As it will be shown later in this paper, Eq. 13 leads to a bigger drop deformation than Eq. 18.
2. With Eq. 13, the simulation must be stopped before the drop moves a distance of $(1/Ca - 1)$ in the z direction. This is because the interfacial tension of the drop will be smaller than zero beyond that location, and not only the simulation will collapse, but also it is not physically possible.

With Eq. 18, on the other hand, the simulation can be extended to the infinity.

In this section, Eq. 18 is adopted in our codes to have some comparisons with the previous researches. It seems that our simulations have very good agreements with the analytical work (Fig. 2), and that a better similarity is achieved when the Reynolds number is smaller. Compared with the previous numerical work [18], our numerical simulations are closer to the theoretical analysis (Fig. 3).

In the rest of this paper, the interfacial tension is calculated by Eq. 13, and simulations are stopped before the capillary force on the drop becomes negative.

IV. RESULTS AND DISCUSSIONS

A. Transient thermocapillary migrations of droplets with large capillary numbers

In this subsection, we simulate the thermocapillary process with the same set of parameters in [18]: $Re = Ma = 50$, $Ca = 0.1$, $\alpha = \lambda = \xi = 0.5$, and $\gamma = 0.25$. The time evolution of migration velocity is shown in Fig. 4 (the solid line). When the capillary number is sufficiently small ($Ca = 0.05$, the dashed line in Fig. 4), the drop will reach a steady migrating state after the initial accelerating process. However, the velocity with $Ca = 0.1$ has an accelerating decrease when $t > 60$, and can not reach a steady state. This result is different from that of [18], in which the steady velocity state was assumed in advance.

The deviation of the drop profile from the sphere for $Ca = 0.1$ at different times is plotted in Fig. 5. It seems that when the drop migrates to the hotter region, the deformation keeps increasing and the drop loses its fore and aft symmetry. At the late stage, the bottom of

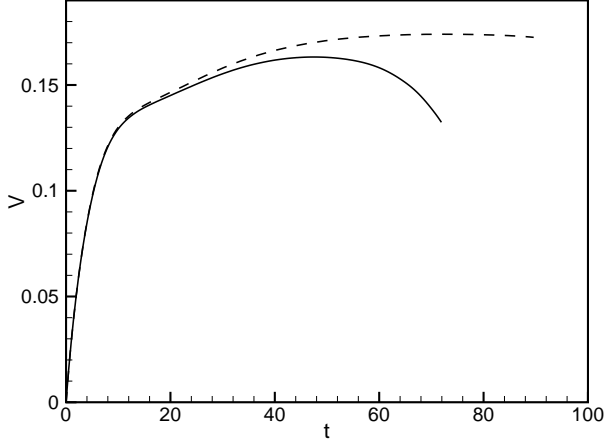


FIG. 4: Time evolution of drop velocity for $Re = Ma = 50$, $\alpha = \lambda = \xi = 0.5$, and $\gamma = 0.25$. $Ca = 0.1$ (solid line); $Ca = 0.05$ (dashed line).

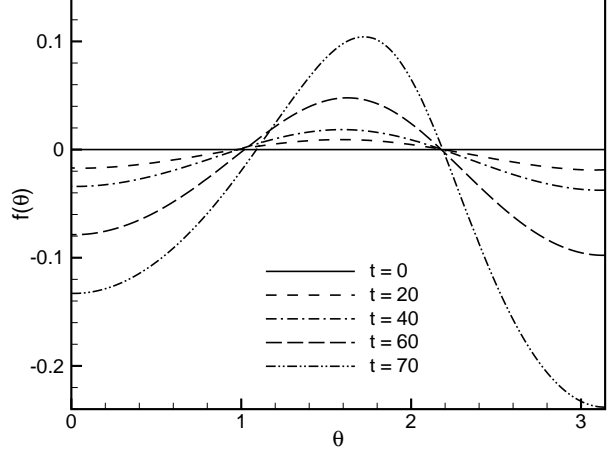


FIG. 5: Deviation of the drop profile from the sphere at indicated times for $Re = Ma = 50$, $Ca = 0.1$, $\alpha = \lambda = \xi = 0.5$, and $\gamma = 0.25$.

the drop becomes flattened, and the drop looks like a cap (Fig. 6(b)). The deformation at $t = 60$ in the current study is about twice bigger than that in the simulation of [18], and even bigger difference at the late stage. There are two reasons for the rapid decline in velocity:

1. Because the drop becomes flatter, the resistance on the drop is increased.
2. Because the distance between the front and rear stagnation points at the late stage is shorter than that in the beginning, their temperature difference also decreases (Fig. 7). As a result, the thermocapillary driving force on the drop becomes smaller.

We also studied the influence of different Re numbers, Ma numbers, and Ca numbers. Some typical results are shown in Figs. 8. With other parameters fixed, the migrating velocity tails off earlier for the larger Reynolds number.

With $Re = Ma = 50$, $Ca = 0.1$, and $\xi = 0.5$, we studied the influence of α , λ and γ . These three parameters play trivial roles in the transient motions of deformable drops. With small α , λ or γ , drops migrate faster (see [5, 25]) and need shorter time to reach the hot regions with near-zero interfacial tensions. As a result, the migration velocities tail off at earlier times.

To sum up, the influence of all other parameters except ξ depends on when the drop migrates to the warm region with very low interfacial tension, in other words, the speed of

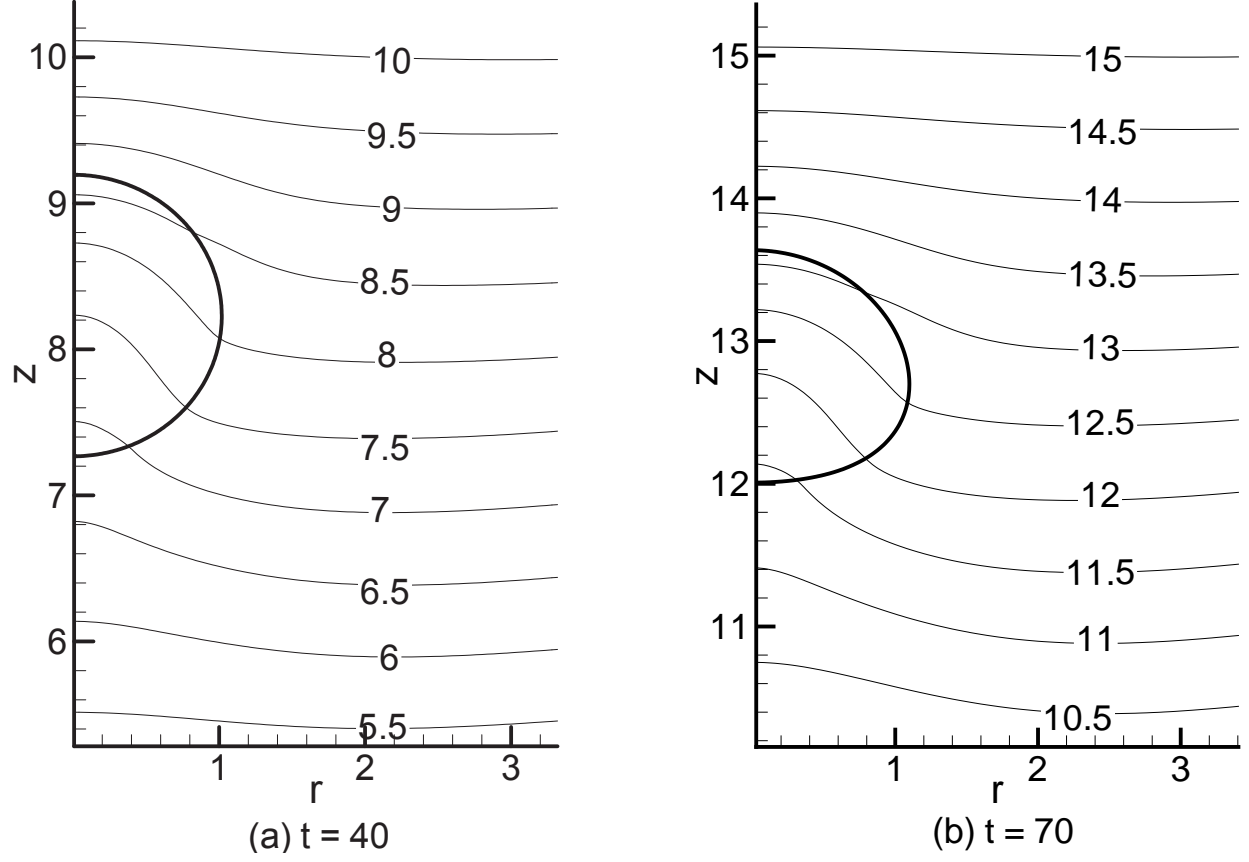


FIG. 6: Isotherms around the drop for $Re = Ma = 50$, $Ca = 0.1$, $\alpha = \lambda = \xi = 0.5$, and $\gamma = 0.25$. a) $t = 40$; b) $t = 70$.

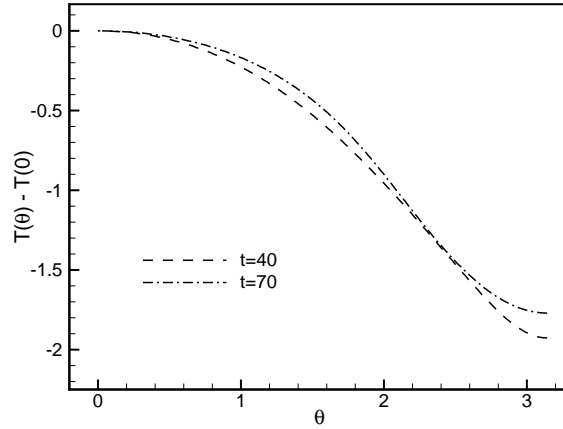


FIG. 7: The temperature distribution on the drop interface for $Re = Ma = 50$, $Ca = 0.1$, $\alpha = \lambda = \xi = 0.5$, and $\gamma = 0.25$ when $t = 40$ and $t = 70$.

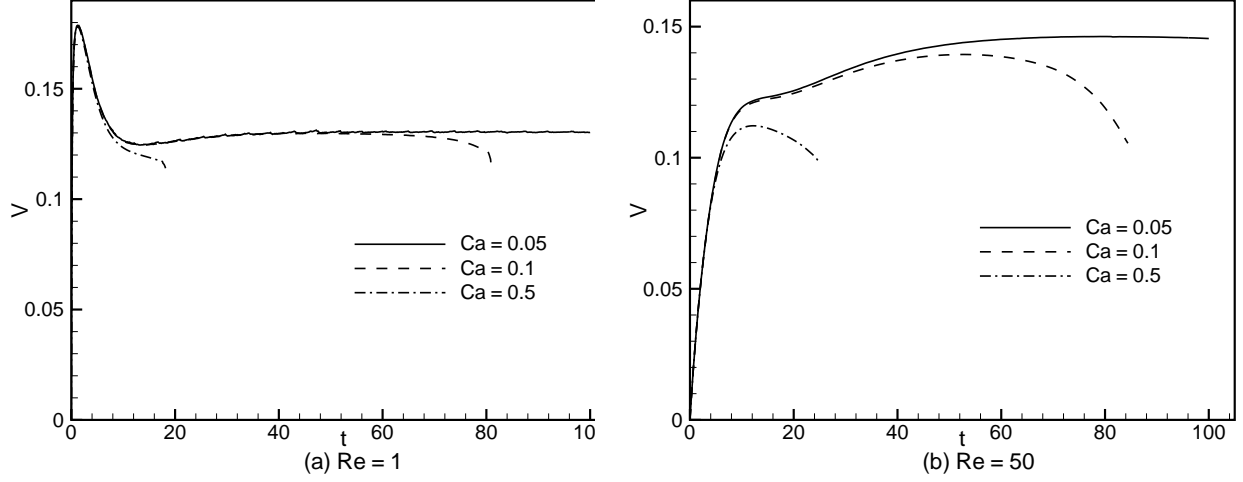


FIG. 8: Time evolutions of the drop velocity for different Ca numbers. $Ma = 100$, $\alpha = \lambda = \xi = 0.5$, and $\gamma = 0.25$. (a) $Re = 1$; (b) $Re = 50$.

the drop. The influence of various parameters on drop speeds has been discussed in detail in our earlier work [5, 26].

B. Influence of density ratio ξ

In the last subsection, densities of drops are always smaller than those of bulk fluids, and we will adopt denser drops ($\xi = 2$) in the following. Several Ca numbers are studied, all other parameters are fixed to make the discussion simpler ($Re = Ma = 50$, $\alpha = \lambda = 0.5$, and $\gamma = 0.25$). The time evolutions of velocities are plotted in Fig. 9, and the most obvious difference from Figs. 4&8 is the continuous increasing trend of velocities. To explain this phenomenon, we focus on the case of $Ca = 0.1$:

1. At the late stage of the migration, the drop profile is elongated in the z direction (Fig. 10(b)), and the temperature difference between the front and rear stagnation points of the drop becomes larger (Fig. 11). As a result, the thermocapillary driving force on the drop becomes larger.
2. Because the drop becomes slender, the resistance on the drop decreases.

To further discuss drop deformations, it is essential to introduce the local capillary number Ca_l to indicate the local magnitude of interfacial tension, which is defined on the moving

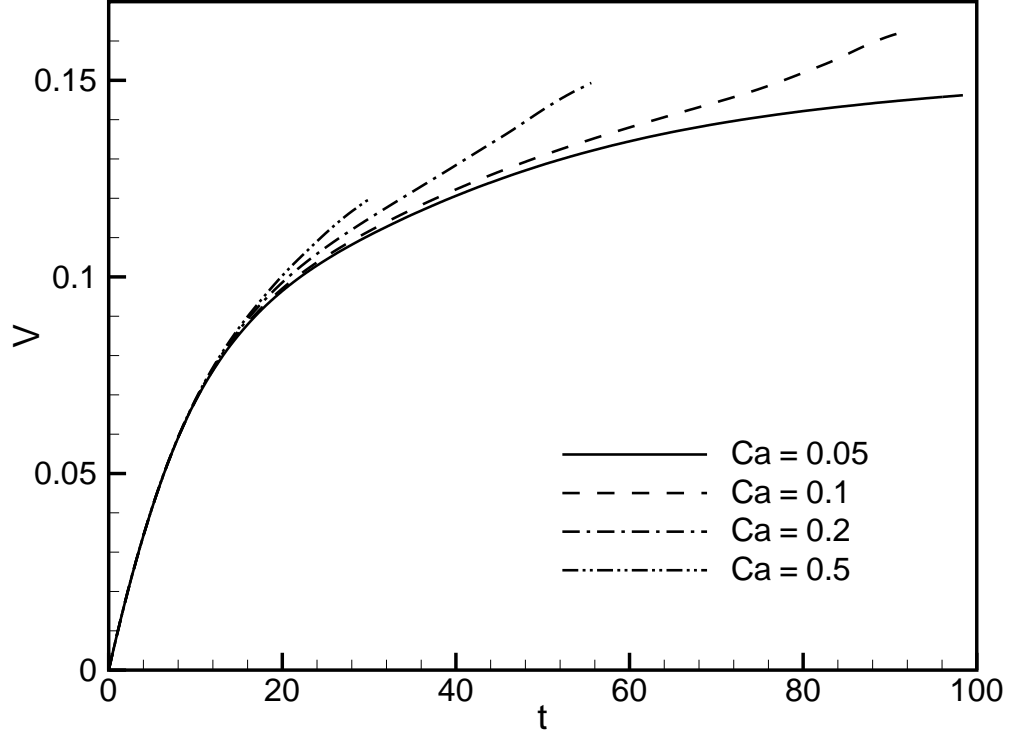


FIG. 9: Time evolutions of drop velocities for different capillary numbers. $Re = 50$, $Ma = 50$, $\alpha = \lambda = 0.5$, $\gamma = 0.25$, and $\xi = 2$.

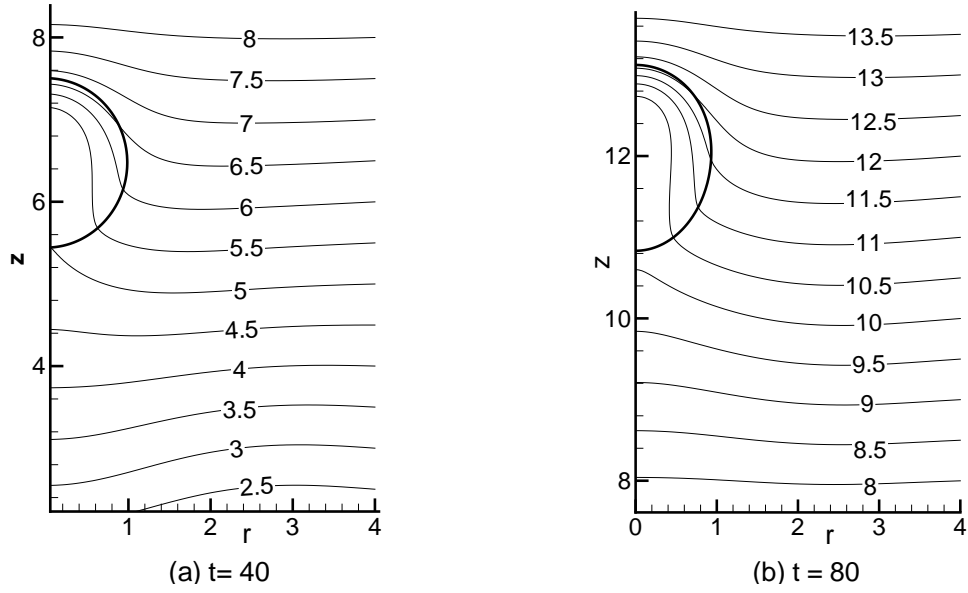


FIG. 10: Isotherms around the drop at $t = 40$ and $t = 80$. $Re = 50$, $Ma = 50$, $Ca = 0.1$, $\alpha = \lambda = 0.5$, $\gamma = 0.25$, and $\xi = 2$.

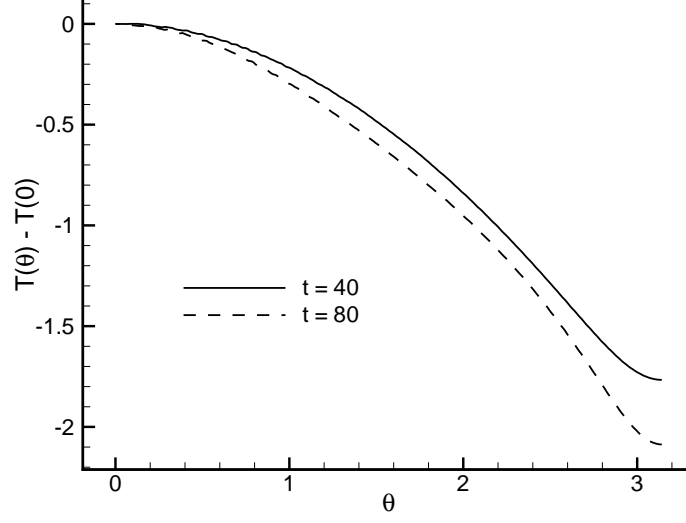


FIG. 11: Temperature distribution on the drop interface at $t = 40$ and $t = 80$. $Re = 50$, $Ma = 50$, $Ca = 0.1$, $\alpha = \lambda = 0.5$, $\gamma = 0.25$, and $\xi = 2$.

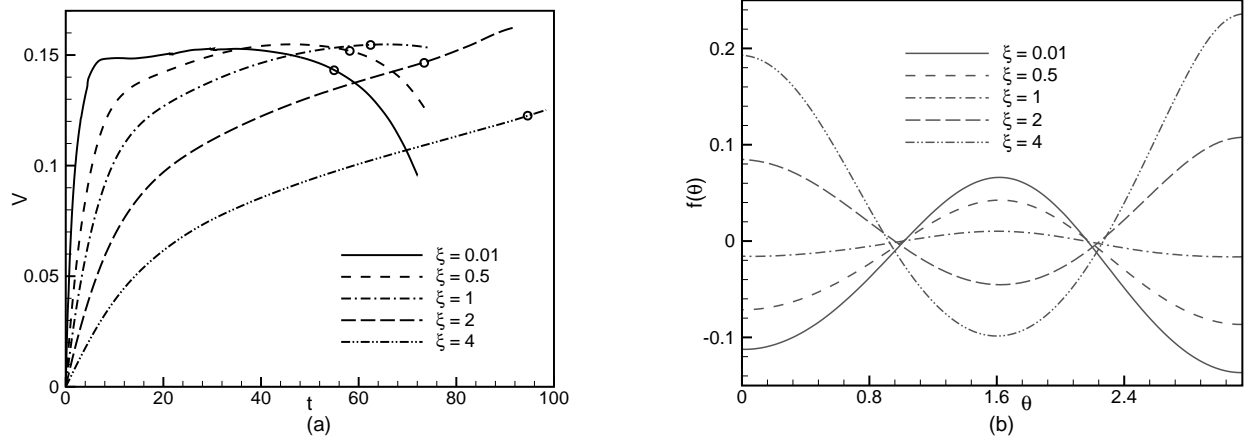


FIG. 12: (a) Time evolutions of drop velocities with different ξ 's, the circles on the velocity curves indicate the locations at $Ca_l = 0.5$; (b) deviations of drop profiles from spheres when $Ca_l = 0.5$. $Re = Ma = 50$, $Ca = 0.1$, $\alpha = \lambda = 0.5$, and $\gamma = 0.25$.

drop center (z_c):

$$Ca_l = \frac{Ca}{1 - Ca(T_{c0} - T_0)} = \frac{Ca}{1 - Ca(z_c - z_0)}, \quad (19)$$

where, T_{c0} represents the initially temperature at z_c . Time evolutions of drop velocities for different ξ 's are plotted in Fig. 12(a). To investigate the ξ influence on deformation, we fixed Ca_l at the value of 0.5, when the drop starts to have an obviously different velocity from that of the non-deformable drop. In the current case ($Ca = 0.1$), $Ca_l = 0.5$ means

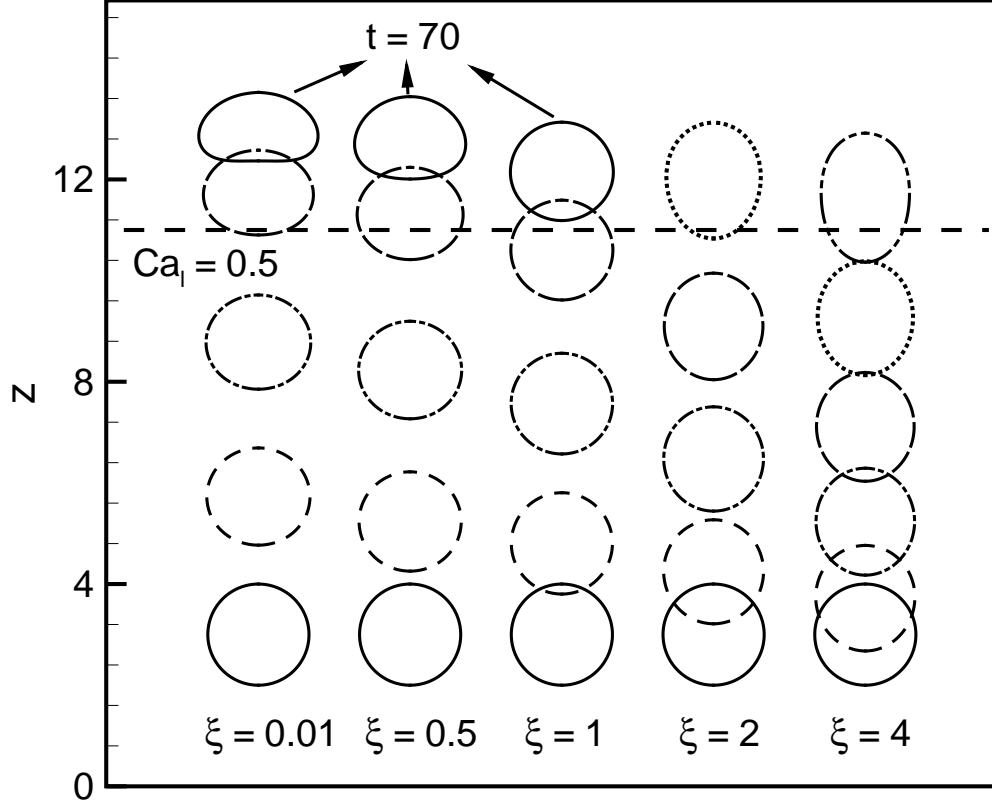


FIG. 13: Time evolutions of drop profiles for different ξ 's, where $Re = Ma = 50$, $Ca = 0.1$, $\alpha = \lambda = 0.5$, and $\gamma = 0.25$. From the bottom to the top, the profiles in each column are corresponding to the time at $t = 0, 20, 40, 60, 80, 100$, respectively.

that the drop migrates a distance of 8 (represented by circles on the curves of Fig. 12(a)). It is found that the drop profile deforms to oblate/slender when ξ is smaller/larger than unit. When the absolute value of $\xi - 1$ becomes larger, the deformation is also larger (Fig. 12(b)). This is consistent in the analytical result (Eq. 17), except that we have larger deformation and Re & Ma numbers here. Fig. 13 presents shape evolutions of drops with different ξ 's.

It should be noticed that only slight deformations on large bubbles ($\xi \sim 10^{-3}$) have been observed in previous space experiments, and no measurable deformations for those heavy drops ($\xi = 1.98$) [3]. The reason for the difference between experiments and simulations might be:

1. Bubbles/Drops in experiments do not migrate to areas with high temperatures, so their interface tensions are still large enough to hold perfect spherical shapes;
2. The assumption for the $\sigma(T)$'s linear dependence on temperature is not correct when

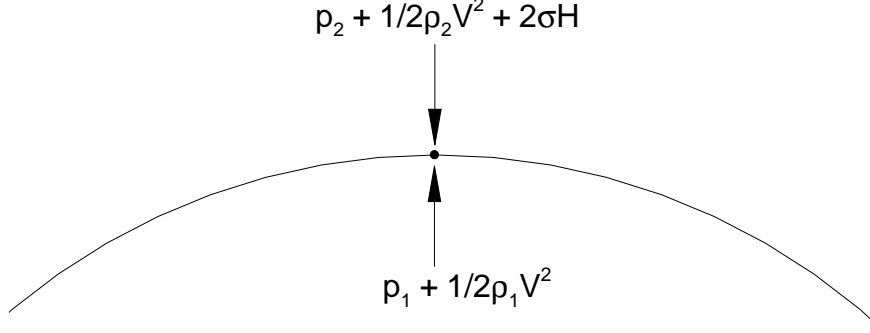


FIG. 14: Sketch of normal stress balance on the stagnation point of the drop.

$\sigma(T) \rightarrow 0$ in experiments (this is, however, the general assumption in most simulations in this field).

To explain the relation between different ξ 's and drop-deforming orientations, a simplified physical explanation is introduced in the following. Only the front stagnation point is studied.

As shown in Fig. 14, the total pressures are $p_2 + \frac{1}{2}\rho_2 V^2$ inside the drop and $p_1 + \frac{1}{2}\rho_1 V^2$ outside the drop; here V is the local fluid velocity, and p_2 and p_1 denote the static pressures at the two sides of the stagnation point, respectively. The extra pressure caused by the interfacial tension is $2\sigma H$ (H is the average curvature). When the interfacial tension is large enough, the normal stress balance on the interface is dominated by the interfacial tension and the droplet keeps spherical. On the other hand, when the interfacial tension becomes small at the hot region (or, $Ca_l > 0.5$), the dynamic pressure becomes dominant:

if $\xi > 1$, the dynamic pressure inside the drop ($\frac{1}{2}\rho_2 V^2$) is larger than that outside ($\frac{1}{2}\rho_1 V^2$).

Larger extra pressure ($2\sigma H$) is needed to balance the normal stress on the interface, so the drop is elongated in the axis direction to have a larger H .

if $\xi < 1$, the dynamic pressure inside is lower than that outside. Smaller extra pressure is needed to balance the normal stress, so the drop is compacted in the axis direction to have a smaller H .

V. CONCLUSIONS

In this work, we found that the influence of deformations on drops is much more complicated than that on bubbles. When the drop density is smaller than the bulk fluid, the

migration velocity will decrease with the increase of the deformation. When the drop density is larger than the bulk fluid, the migration velocity will increase with the increase of the deformation. With the assumption adopted in this paper, we believe that in the hot region the drop will always start to deform, and there is no way to have any constant migrating velocity. Hence, keeping Ca and Ca_l small throughout simulations is the only possible way for the drop to keep spherical and reach the steady migrating state.

All the discussions above are based on the assumption of the linear temperature dependence of the interfacial tension. More complicated temperature dependence will be used in the future work, and variations of physical properties with the temperature will also be considered.

Acknowledgments

This project is supported by the Knowledge Innovation Program of the Chinese Academy of Sciences, Grant No. KJCX2-YW-L08.

-
- [1] Ratke L, Korekt G. Solidification of Al-Pb-base alloys in low gravity. *Z Metallkde*, 2000, 91: 919-927
 - [2] Ostrach S. Low gravity fluid flows. *Annu Rev Fluid Mech*, 1982, 14:13-345
 - [3] Hadland P H, Balasubramaniam R, Wozniak G, et al. Thermocapillary migration of bubbles and drops at moderate to large Marangoni number and moderate Reynolds number in reduced gravity. *Exp Fluids*, 1999, 26:240-248
 - [4] Hoyer W, Kaban I. Experimental and calculated liquid-liquid interface tension in dimixing metal alloys. *Rare Met*, 2006, 25(5):452-456
 - [5] Yin Z H, Gao P, Hu W R, et al. Thermocapillary migration of nondeformable drops. *Phys Fluids*, 2008, 20: 082101
 - [6] Carlberg T, Fredriksson H. The influence of microgravity on the solidification of Zn-Bi immiscible alloys. *Metal Trans A*, 1980, 11(10):1665-1676
 - [7] Li H L, Zhao J Z. Convective effect on the microstructure evolution during a liquid-liquid decomposition. *Appl Phys Lett*, 2008, 92(24):241902

- [8] Gurgel A, Moura M C P A, Dantas T N C, et al. A review on chemical flooding methods applied in enhanced oil recovery. *Braz J Pet Gas*, 2008, 2(2):83-95
- [9] Xia H F, Liu R Q, Ju Y, et al. Mechanism of betaine surfactant solution on residual oil after water flooding in ultralow interfacial tension. *J Daqing Pet Inst*, 2006, 30(6):24-27(in Chinese)
- [10] Lyford P A, Pratt H R C, Shallcross D C, et al. The marangoni effect and enhanced oil recovery Part 1. Porous media studies. *Can J Chem Eng*, 1998, 76(2):167-174
- [11] Lyford P A, Pratt H R C, Shallcross D C, et al. The marangoni effect and enhanced oil recovery Part 2. Interfacial tension and drop instability. *Can J Chem Eng*, 1998, 76(2): 175-182
- [12] Morrow N R, Mason G. Recovery of oil by spontaneous imbibition. *Curr Opin Coll Int Sci*, 2001, 6(4):321-337
- [13] Young N O, Goldstein J S, Block M J. The motion of bubbles in a vertical temperature gradient. *J Fluid Mech*, 1959, 11: 350-356
- [14] Subramanian R S, and Balasubramaniam R. *The Motion of Bubbles and Drops in Reduced Gravity*. Cambridge:Cambridge University Press, 2001
- [15] Subramanian R S, Balasubramaniam R, Wozniak G. *Fluid Mechanics of Bubbles and Drops*. London: Taylor & Francis, 2002:149-177
- [16] Balasubramaniam R, Chai A. Thermocapillary migration of droplets: an exact solution for small marangoni numbers. *J Colloid Interface Sci*, 1987, 119:531-538
- [17] Haj-Hariri H, Nadim A, Borhan A. Effect of inertia on the thermocapillary velocity of a drop. *J Colloid Interface Sci*, 1990, 140(1):277-286
- [18] Haj-Hariri H, Shi Q, Borhan A. Thermocapillary motion of deformable drops at finite Reynolds and Marangoni numbers. *Phys Fluids*, 1997, 9(4):845-855
- [19] Welch S W J. Transient thermocapillary migration of deformable bubbles. *J Colloid Interface Sci*, 1998, 208: 500-508
- [20] Unverdi S O, Tryggvason G. A front-tracking method for viscous, incompressible, multi-fluid flows. *J Comput Phys*, 1992, 100:25-37
- [21] Tryggvason G, Bunner B, Esmaeeli A, et al. A front-tracking method for the computations of multiphase flow. *J Comput Phys*, 2001, 169:708-759
- [22] Kreyszig E. *Differential Geometry*. New York: Dover Publications, 1991
- [23] Hua J S, Lou J. Numerical simulation of bubble rising in viscous liquid. *J Comput Phys*, 2007, 222:769-795

- [24] Chorin A J. A numerical method for solving incompressible viscous flow problems. J Comput Phys, 1967, 2:12-26
- [25] Nas S. Computational Investigation of Thermocapillary Migration of Bubbles and Drops in Zero Gravity. Doctor Dissertation. Michigan: The University of Michigan, 1995
- [26] Gao P. Numerical Investigation of the Drop Thermocapillary Migration. Doctor Dissertation(in Chinese). Beijing: Graduate University of Chinese Academy of Science, 2007
- [27] Moldover M R. Interfacial tension of fluids near critical points and two-scale-factor universality. Phys Rev A, 1985, 31(2):1022-1033